Optics Letters

Silicon-on-insulator free-carrier injection modulators for the mid-infrared

M. Nedeljkovic,[1,*] C. G. Littlejohns,[1,2] A. Z. Khokhar,[1] M. Banakar,[1] W. Cao,[1] J. Soler Penades,[1] D. T. Tran,[1] F. Y. Gardes,[1] D. J. Thomson,[1] G. T. Reed,[1] H. Wang,[2] and G. Z. Mashanovich[1]

[1]Optoelectronics Research Centre, University of Southampton, Southampton SO17 1BJ, UK
[2]Silicon Technologies Centre of Excellence, Nanyang Technological University, 639798 Singapore, Singapore
*Corresponding author: m.nedeljkovic@soton.ac.uk

Received 6 November 2018; accepted 1 December 2018; posted 7 December 2018 (Doc. ID 351242); published 11 February 2019

Experimental demonstrations of silicon-on-insulator waveguide-based free-carrier effect modulators operating at 3.8 μm are presented. PIN diodes are used to inject carriers into the waveguides, and are configured to (a) use free-carrier electroabsorption to create a variable optical attenuator with 34 dB modulation depth and (b) use free-carrier electrorefraction with the PIN diodes acting as phase shifters in a Mach–Zehnder interferometer, achieving a $V_\pi L_\pi$ of 0.052 V · mm and a DC modulation depth of 22 dB. Modulation is demonstrated at data rates up to 125 Mbit/s.

https://doi.org/10.1364/OL.44.000915

For several years, there has been rapid progress in the development of a library of silicon-on-insulator (SOI) waveguide-based building blocks for photonic integrated circuits (PICs) that can operate in the mid-infrared (mid-IR), since the mid-IR portion of the electromagnetic spectrum is of great interest for a variety of practical applications [1]. Although much of the research effort in this field has been devoted to developing alternative material platforms, SOI is transparent at approximately 1.1–2.7 and 3.0–4.0 μm [1,2] and, if the waveguide is engineered for high mode confinement in Si instead of SiO_2, it can even be used up to 6 μm [3]. If the SiO_2 lower cladding is removed, SOI can be used up to nearly 8 μm [4]. Because of the wide use of SOI for near-infrared (NIR) silicon photonics, SOI should still be considered to be the first choice when building PICs that are required to operate at wavelengths at which it is transparent.

To date, one aspect of mid-IR SOI technology that has not been adequately explored is effective modulation, which is a key functionality in many PICs. In the SOI platform, modulators exploiting the injection, depletion, or accumulation of free carriers have become dominant in the NIR [5–7]. We have recently demonstrated depletion type modulators operating at 20 Gbit/s in Ref. [8] and, to the best of our knowledge, to date, the longest wavelength at which silicon-based free-carrier modulators have been demonstrated is 2165 nm [9]. In the mid-IR intensity modulation or phase shifting may be important for circuits designed for free-space communication, signal processing functionality (e.g., acting as a broadband on-chip "chopper" in a lock in amplifier system), phased arrays for beam steering [10], or switching such as in circuits such as the Fourier-transform spectrometers proposed in Ref. [11]. We previously proposed predictions for the sizes of the free-carrier electroabsorption and electrorefraction effects in Si in Ref. [12] but, to date, these equations have not been experimentally verified beyond 2 μm [13]. From Ref. [12], the strength of the free-carrier effect is expected to be approximately proportional to the square of the wavelength so that, for the same change in carrier concentration, mid-IR modulators should be more effective than NIR modulators. In this Letter, therefore, we have designed and fabricated free-carrier injection modulators working at ∼3.8 μm (near the edge of SOI's transparency range). In Ref. [14], we have presented an initial demonstration of an SOI electroabsorption modulator operating under DC conditions. Here we also show the operation of an electrorefraction modulator, demonstrate AC modulation of both, and present a thorough investigation of the experimental device performance and compare it against the predictions of Ref. [12].

Design and simulation: Two types of free-carrier modulators were designed, both exploiting free-carrier injection into waveguides using a PIN diode. The first modulator operates as a variable optical attenuator (VOA) in which carriers injected into the waveguide core absorb the propagating light. The second modulator was an asymmetric Mach–Zehnder interferometer (MZI) with PIN diodes placed in each arm, in which carriers are injected into the waveguide in one of the MZI arms in order to change the refractive index of the Si in the waveguide core, creating a phase shift in the waveguide arm. The MZI then converts the phase shift into an intensity shift.

Modulator layout designs: The electroabsorption modulator is simply a waveguide with an integrated PIN diode. In order to reduce the on-chip length of the device, the waveguide and PIN diode were wrapped into a spiral shape, as shown in the

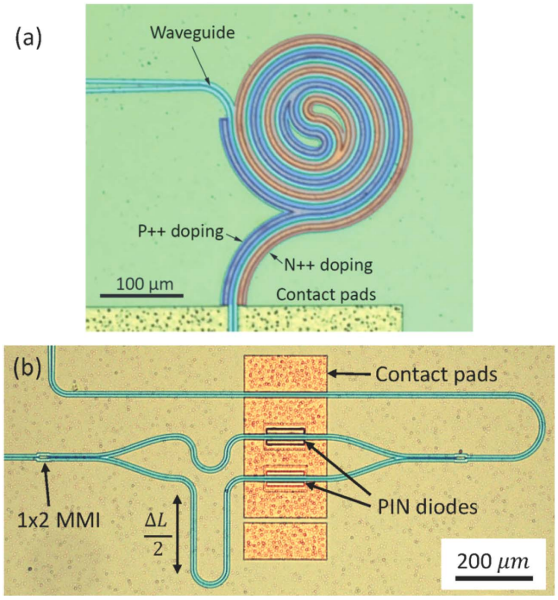

Fig. 1. (a) Optical microscope image of the spiral-shaped PIN electroabsorption modulator. P++ doped areas have been artificially colored in red, and N++ doped areas have been colored in blue. (b) Optical microscope image of the MZI electrorefraction type modulator.

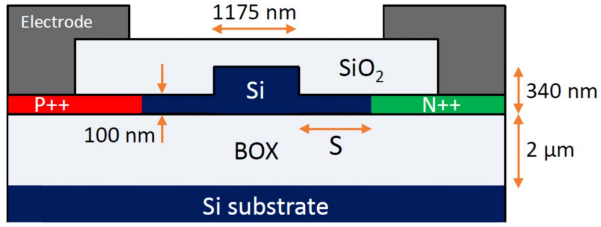

Fig. 2. Schematic cross section of the SOI PIN diode.

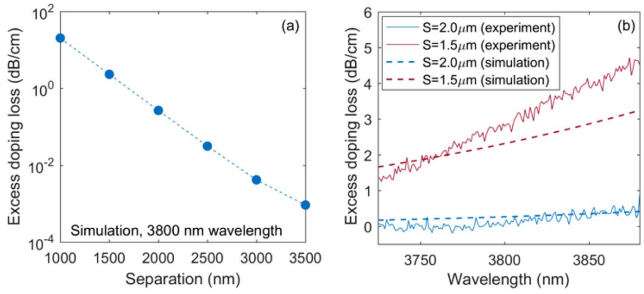

Fig. 3. (a) Simulated propagation loss of the PIN junction integrated waveguide (whose cross section is shown in Fig. 2) with varying doping separation (S) at a wavelength of 3.8 μm. (b) The solid red and blue lines show experimentally measured waveguide loss spectra due to Ohmic contact doping with separations (S) of 1.5 and 2.0 μm, respectively. The dashed lines show the simulated doping loss for waveguides with the same nominal dimensions.

optical microscope image in Fig. 1(a). In this way, a 2.0 mm long diode was wrapped into a circular area with a diameter of 230 μm. The minimum waveguide bend radius at the center of the spiral was 20 μm, and the edge-to-edge separation between waveguides in adjacent loops of the spiral was 16 μm; thus, there was sufficient space to position the doping through oxide vias and metal tracks between the waveguides. The electrorefraction modulator MZI is shown in Fig. 1(b). In this case, the PIN diode length is only 100 μm, and there is a 350 μm arm length difference (ΔL) between the two MZI arms. In both implementations, the layouts were designed so that the metal electrodes do not pass directly over the waveguides, as at this wavelength the 1 μm thick top cladding is too thin to isolate the waveguide mode from seeing the metal.

PIN diode cross section: The PIN diodes were designed to have a cross section, as shown in Fig. 2. The SOI wafers had a Si device layer thickness of 340 nm, the buried oxide layer was 2 μm thick, the etch depth was 140 nm, and the waveguide width was 1175 nm. The layer thicknesses were chosen for compatibility with commercial foundry services. Simulations using the Lumerical Mode Solutions software EME solver [15] showed that these waveguides would support the fundamental TE mode only. The SiO_2 top cladding thickness was 1 μm. The P++ and N++ Ohmic contact regions had doping concentrations of $1e20$ cm^{-3} of boron and $9e19$ cm^{-3} of phosphorus. The Si had an n-type background doping of $1.5e17$ cm^{-3}.

The most important design parameter was the separation of the Ohmic contact regions from the waveguide core, marked S on Fig. 2. When S is small, these highly doped regions overlap with the waveguide optical mode and contribute excess loss and, since the waveguide mode area scales with the wavelength, the Ohmic contacts must be placed further away from the waveguide core than in an equivalent NIR device. However, as S increases, both the volume of the intrinsic region into which carriers are injected and the PIN junction resistance increase, reducing the modulator efficiency and frequency bandwidth.

Figure 3(a) shows the excess loss due to Ohmic contact doping for varying S, simulated using Lumerical Mode Solutions. The absorption coefficient and the refractive index of the implanted P++ and N++ regions due to implanted carriers were calculated using Eqs. (4) and (5) and the parameters from Table 1 from Ref. [12], where predictions of this relationship are given. Since Ref. [12] gives parameters at 3.5 and 4.0 μm, we used linear interpolation to approximate the parameters at 3.8 μm, giving the following equations:

$$\Delta\alpha = 1.69 \times 10^{-21}\Delta N_e^{1.23} + 5.68 \times 10^{-20}\Delta N_h^{1.15}, \quad \textbf{(1)}$$

$$\Delta n = 7.13 \times 10^{-21}\Delta N_e^{0.989} + 9.71 \times 10^{-18}\Delta N_h^{0.837}. \quad \textbf{(2)}$$

$\Delta\alpha$ is the change in the absorption coefficient (cm^{-1}), Δn is the change in refractive index, and ΔN_e and ΔN_h are the changes in electron and hole concentrations (cm^{-3}), respectively. Based on the simulated losses, we designed devices with S between 1.5 and 3.5 μm.

Experimental work and results: The devices were fabricated at the University of Southampton. E-beam lithography was used for all patterning steps. The waveguides, gratings, and through oxide vias were etched by inductively coupled plasma (ICP) etching. Ion implantation was carried out at

the University of Surrey's Ion Beam Centre and, after fabrication, the implanted ion concentrations were verified by SIMS measurements. The electrodes consisted of a Ti, TiN, Al, Ti, and TiN stack, which was deposited by sputtering and patterned by ICP etching.

Experimental setup: We characterized the devices using our mid-IR experimental setup, which uses a quantum cascade laser that is tunable from 3715 to 3888 nm, and a custom-built Vigo Systems HgCdTe PVI-4TE-4 photodetector, which has a −3 dB bandwidth greater than 400 MHz. The optical part of the setup is described in much greater detail in Ref. [16].

Passive device characterization: The waveguide loss was measured to be 11.5 dB/cm at 3720 nm, rising to 15.0 dB/cm at 3880 nm. A large part of this high loss is due to the $1.5e17$ cm^{-3} n-type background doping, which we estimated using simulations would cause 7.0 dB/cm of loss at 3720 nm and 6.7 dB/cm at 3880 nm (since the mode confinement in the Si shrinks). Furthermore, the increasing loss across this range is likely the combined result of increasing the substrate leakage through the BOX, increasing mode interaction with the waveguide sidewalls, increasing the SiO_2 absorption coefficient [17], and increasing the mode overlap with the lossy SiO_2 cladding. Indeed, simulations indicate that the substrate leakage would be expected to increase from 1.3 to 3.2 dB/cm over the same wavelength range, and the SiO_2 absorption loss would increase from 1.5 to 3.2 dB/cm.

The excess loss due to doping of the Ohmic contact regions was obtained by measuring the transmission through different waveguides of the same length, but with different lengths of doping running alongside the waveguide with an edge-to-edge separation of S, with the cross section shown in Fig. 2. The wavelength dependencies of the doping with $S = 1.5$ μm and $S = 2.0$ μm are shown in Fig. 3(b), together with simulated loss spectra for the same geometries. With $S = 2.0$ μm, there is almost negligible loss, whereas with $S = 1.5$ μm the loss increases to between 1 and 5 dB/cm, which may be tolerable for PIN diodes with lengths on the order of millimeters. The simulations of the free-carrier absorption due to doping appear to agree relatively well with the experimental measurements.

The insertion loss of the spiral waveguide without Ohmic contact doping, vias, or metal, was 0.8–1.5 dB. When the full PIN diode spiral was fabricated with $S = 1.5$ μm the insertion loss increased to 1.7–3.1 dB. The insertion loss of the MZI modulator with $S = 1.5$ μm was 2.9 dB at 3779 nm. In this device, there was a negligible difference between the insertion losses of the passive MZI and the full MZI with PIN diodes, due to the short 100 μm diode length, suggesting that in this device the doping could be positioned even closer to the waveguide with acceptable loss.

DC electro-optical characterization: The DC electro-optical performance of both the VOA and the MZI were characterized by applying DC forward bias voltages between 0 and 2 V. Figure 4(a) shows the relationship between the injection current per unit diode length (in A/cm) and the absorption due to injected carries (in dB/cm) for spiral VOA devices with varying S. The strong impact of S on the modulation efficiency is clear, with the $S = 1.5$ μm device having the highest efficiency of 380 dB/A and, in its 2 mm length, the device achieves a 34 dB modulation depth with a 2 V bias.

The measured transmission spectra of the MZI with $S = 1.5$ μm are plotted in Fig. 4(c) for varying forward bias voltages

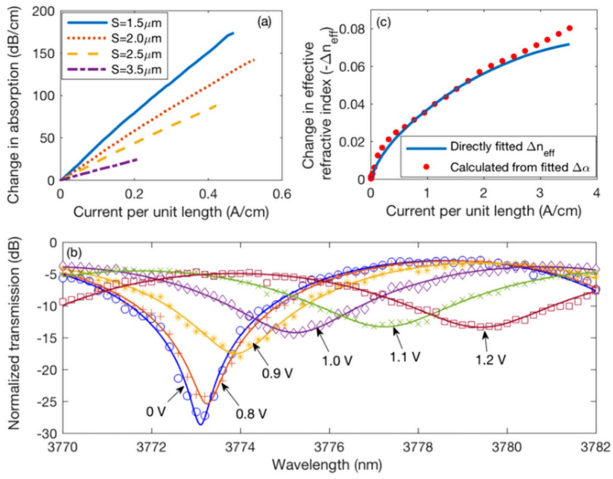

Fig. 4. (a) Measured absorption introduced into spiral-shaped electroabsorption modulators at a 3.8 μm wavelength with varying forward bias current, plotted for devices with varying contact separation (S). The current and absorption coefficient have both been divided by the PIN diode length, which is 2.0 mm for all of these devices. (b) Measured change in effective refractive index extracted from the transmission spectra of the MZI modulator, plotted against varying forward bias current per unit length applied to the 100 μm long phase shifter. (c) Normalized transmission spectra of the MZI modulator for varying applied forward bias voltage applied to the PIN diode in one arm. The markers show the measured points, and the solid lines show fitted theoretical MZI transmission curves. The device shown in (b) and (c) used contact separation $S = 1.5$ μm.

applied to only one arm of the MZI. The maximum modulation depth achieved is 22.2 dB. Note that transmission spectra have only been plotted for some of the bias voltages for clarity of the figure. The corresponding change in the effective refractive index and the absorption coefficient at each bias point have been extracted by fitting theoretical MZI transmission curves to the experimental data, with the form [18]

$$P_{\text{out}} = \frac{P_{\text{in}}}{4}(\tau_1^2 + \tau_2^2 + 2\tau_1\tau_1 \cos(\Delta\varphi)). \tag{3}$$

P_{in} is the optical input power, P_{out} is the output power, and $\tau_{\text{i}}^2 = \exp(-\alpha_i L)$, with α_i being the absorption coefficient in each arm and L_i being the length of each arm. $\Delta\varphi$ is the phase difference between the two arms, with the phase given by $\varphi = 2\pi n_{\text{eff}}/L$, where n_{eff} is the effective refractive index. The extracted change of effective refractive index (Δn_{eff}) has been plotted in Fig. 4(b) as a function of the injection current per unit diode length. The $V_\pi L_\pi$ figure of merit of the MZI modulator is 0.052 V.mm at 2 V bias.

In order to confirm the validity of Eqs. (1) and (2), we have also used the fitted $\Delta\alpha$ at each bias point to calculate the corresponding change in carrier concentration ΔN from Eq. (1), assuming that in the intrinsic region $\Delta N = \Delta N_e = \Delta N_h$. From this ΔN, we have then calculated the predicted Δn using Eq. (2) and plotted it on Fig. 4(b). The figure shows that the experimentally fitted Δn_{eff} agrees well with the Δn calculated from the fitted $\Delta\alpha$, indicating that Eqs. (1) and (2) are consistent (for the same unknown free-carrier concentration).

AC electro-optical characterization: To characterize the AC response of the modulator, it was driven by a pseudo random

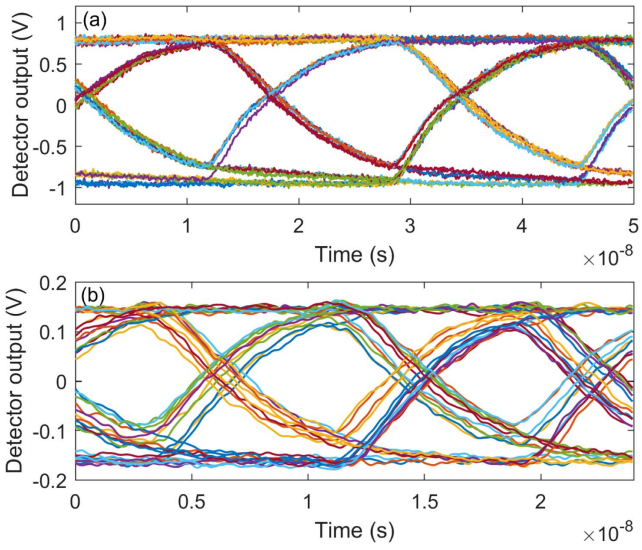

Fig. 5. (a) Eye diagrams of (a) electroabsorption modulator at 60 Mbit/s and (b) MZI modulator at 125 Mbit/s.

bit sequence with $2^7 - 1$ bit length, while a DC power supply provides a voltage offset, and the DC and AC signals are combined by a bias-tee. The VOA modulator with $S = 1.5$ μm was driven by a signal with 0.5 V amplitude and 1 V offset at data rates up to 60 Mbit/s. The resulting open eye diagram is shown in Fig. 5(a). The photodetector used for the measurements is AC coupled and, therefore, does not measure the DC component of the optical signal, making it impossible to extract the extinction ratio of the diagram. The y-axis of the eye diagram is the photodetector output in V.

The MZI modulator was driven in a push-pull configuration with a signal with 0.25 V amplitude and 0.75 V offset using the PIN diodes in both MZI arms and, in this configuration, an open eye diagram was measured at up to 125 Mbit/s, as shown in Fig. 5(b).

In summary, we have demonstrated SOI carrier junction electroabsorption and electrorefraction modulators for a 3.8 μm wavelength. The electroabsorption modulator achieves a DC modulation depth of 34 dB and an AC data rate of 60 Mbit/s, while the electrorefraction modulator achieves a DC modulation depth of 22.2 dB with a $V_\pi L_\pi$ of 0.052 V.mm and an AC data rate of 125 Mbit/s. The $V_\pi L_\pi$ figure of merit compares favorably to similar published NIR devices [7,19].

The MZI modulator measurements indicate that the free-carrier effect equations for this wavelength in Ref. [12] accurately predict the correlation between the absorption coefficient and refractive index changes due to a change in free-carrier concentration, while the measurements of excess loss from doping indicate that the equations also reasonably accurately predict the absolute value of the free-carrier absorption.

Funding. Engineering and Physical Sciences Research Council (EPSRC) (EP/N00762X/1, EP/N013247/1, EP/R004951/1); National Research Foundation Singapore (NRF) (NRF-CRP12-2013-04); Royal Academy of Engineering (RF201617/16/33); Royal Society (D. J. Thomson URF).

Acknowledgment. All data supporting this study are openly available at https://doi.org/10.5258/SOTON/D0740.

REFERENCES

1. R. Soref, Nat. Photonics **4**, 495 (2010).
2. G. Z. Mashanovich, M. M. Milosevic, M. Nedeljkovic, N. Owens, B. Xiong, E. J. Teo, and Y. Hu, Opt. Express **19**, 7112 (2011).
3. S. A. Miller, M. Yu, X. Ji, A. G. Griffith, J. Cardenas, A. L. Gaeta, and M. Lipson, Optica **4**, 707 (2017).
4. J. S. Penadés, A. Sánchez-Postigo, M. Nedeljkovic, A. Ortega-Moñux, J. G. Wangüemert-Pérez, Y. Xu, R. Halir, Z. Qu, A. Z. Khokhar, A. Osman, W. Cao, C. G. Littlejohns, P. Cheben, I. Molina-Fernández, and G. Z. Mashanovich, Opt. Lett. **43**, 795 (2018).
5. G. T. Reed, G. Mashanovich, F. Y. Gardes, and D. J. Thomson, Nat. Photonics **4**, 518 (2010).
6. D. J. Thomson, F. Y. Gardes, J. M. Fedeli, S. Zlatanovic, Y. Hu, B. P. P. Kuo, E. Myslivets, N. Alic, S. Radic, G. Z. Mashanovich, and G. T. Reed, IEEE Photonics Technol. Lett. **24**, 234 (2012).
7. W. M. J. Green, M. J. Rooks, L. Sekaric, and Y. A. Vlasov, Opt. Express **15**, 17106 (2007).
8. W. Cao, D. Hagan, D. J. Thomson, M. Nedeljkovic, C. G. Littlejohns, A. Knights, S.-U. Alam, J. Wang, F. Gardes, W. Zhang, S. Liu, K. Li, M. S. Rouifed, G. Xin, W. Wang, H. Wang, G. T. Reed, and G. Z. Mashanovich, Optica **5**, 1055 (2018).
9. M. A. Van Camp, S. Assefa, D. M. Gill, T. Barwicz, S. M. Shank, P. M. Rice, T. Topuria, and W. M. J. Green, Opt. Express **20**, 28009 (2012).
10. M. J. R. Heck, Nanophotonics **6**, 93 (2017).
11. D. M. Kita, H. Lin, A. Agarwal, K. Richardson, I. Luzinov, T. Gu, and J. Hu, IEEE J. Sel. Top. Quantum Electron. **23**, 340 (2017).
12. M. Nedeljkovic, R. Soref, and G. Z. Mashanovich, IEEE Photonics J. **3**, 1171 (2011).
13. D. E. Hagan and A. P. Knights, J. Opt. **19**, 025801 (2017).
14. G. Z. Mashanovich, M. Nedeljkovic, J. Soler-Penades, Z. Qu, W. Cao, A. Osman, Y. Wu, C. J. Stirling, Y. Qi, Y. X. Cheng, L. Reid, C. G. Littlejohns, J. Kang, Z. Zhao, M. Takenaka, T. Li, Z. Zhou, F. Y. Gardes, D. J. Thomson, and G. T. Reed, Opt. Mater. Express **8**, 2276 (2018).
15. Lumerical Solutions Inc., https://www.lumerical.com/.
16. M. Nedeljkovic, "Silicon photonic modulators for the mid-infrared," Ph. D. dissertation (University of Southampton, 2013).
17. R. Kitamura, L. Pilon, and M. Jonasz, Appl. Opt. **46**, 8118 (2007).
18. G. T. Reed, *Silicon Photonics: The State of the Art* (Wiley, 2008).
19. L. Yang, H. Chen, and J. Ding, *9th International Conference on Group IV Photonics (GFP)* (2012), pp. 129–131.